Tsunamigenic submarine landslides along the Xauen-Tofiño banks in the Alboran Sea (Western Mediterranean Sea)

Mathieu Rodriguez, Clément Maleuvre, Martin Jollivet-Castelot, Elia d'Acremont, Alain Rabaute, Manfred Lafosse, Gemma Ercilla, Juan-Tomás Vázquez, Belén Alonso, Abdellah Ammar, et al.

HAL Id: insu-03641966

https://insu.hal.science/insu-03641966

Submitted on 14 Apr 2022

Tsunamigenic submarine landslides along the Xauen–Tofiño banks in the Alboran Sea (Western Mediterranean Sea)

Mathieu Rodriguez,[1] Clément Maleuvre,[1,2,3,4] Martin Jollivet-Castelot,[2,3,5]
Elia d'Acremont,[2,3] Alain Rabaute,[2,3] Manfred Lafosse,[2,3] Gemma Ercilla,[6]
Juan-Tomás Vázquez,[7] Belén Alonso,[6] Abdellah Ammar[8] and Christian Gorini[2,3]

[1]*Laboratoire de Géologie de l'Ecole Normale Supérieure de Paris; PSL Research University, CNRS UMR* 8538, 24 *rue Lhomond, F-75005 Paris, France.* E-mail: rodriguez@geologie.ens.fr
[2]*Sorbonne Universités, UPMC Université Paris* 6, *UMR* 7193, *ISTeP, F-75005 Paris, France*
[3]*CNRS, UMR* 7193, *ISTeP, F-75005 Paris, France*
[4]*Ecole Nationale Supérieure de Géologie,* 2 *rue du Doyen Marcel Roubault, TSA* 70605, *F-54518 Vandoeuvre-les-Nancy, France*
[5]*LOG-UMR* 8187, *Université de Lille* 1, *Bâtiment SN5, Cité Scientifique, F-59655 Villeneuve d'Ascq, France*
[6]*Instituto de Ciencias del Mar, CSIC, Passeig Marítim de la Barceloneta* 37–49, *E-08003 Barcelona, Spain*
[7]*Instituto Español de Oceanografía, Centro Oceanográfico de Málaga, Puerto Pesquero s/n, E-29640 Fuengirola, Spain*
[8]*Faculté des Sciences, Université Mohammed V,* 1014 *RP Rabat, Morocco*

SUMMARY

The active Eurasia–Nubia plate boundary runs across the Alboran Sea in the Western Mediterranean Sea, where the connection between the Atlantic and Mediterranean water masses occurs. Earthquakes above magnitude $M_w > 6$ may favour the occurrence of landslides within contouritic drifts in the Alboran Sea. A compilation of recent multibeam data reveals for the first time the distribution of slope failures along the Xauen–Tofiño banks, in the southern Alboran Sea. Here, we provide a detailed mapping and description of the morphology of eight Holocene landslides, including volume estimations of the failed mass and the related mass transport deposits (MTDs). The most voluminous landslide mobilized ∼0.5 km^3 of sediment at the initial stage of slope failure, and formed a ∼2.2–5.6 km^3 MTD. A finite-difference numerical model, assimilating the landslide to a granular flow, simulates tsunami generation and propagation for a slide similar to the most voluminous one. Simulations show that the coastline of Al Hoceima may be impacted by a ∼0.5-m-high tsunami wave, whereas the coastline of Al Jebha may be impacted by a ∼1-m-high tsunami wave, only ∼13 min after sediment failure. The 0.2-m-high tsunami waves may impact the southern Spanish coast of the Iberian Peninsula ∼20 min after slide initiation. Although the elevations of the modeled tsunami waves are modest, landslides from the Xauen–Tofiño banks may represent a more dangerous source of tsunami in some parts of the Moroccan coast than earthquakes.

Key words: Tsunamis; Submarine landslides; Submarine tectonics and volcanism; Africa.

1 INTRODUCTION

Submarine landslides can damage seabed infrastructures and generate significant tsunamis (Masson *et al.* 2006), such as the deadly Papua-New Guinea event in 1998, which caused more than 2200 casualties (Tappin *et al.* 2001). Tsunamis are long gravity waves (with wavelength λ ∼ 100 km and period in the 10–30 min range; i.e. shallow-water waves) generated by an impulsive perturbation of the seafloor, with a phase velocity $c = \sqrt{gh}$ at long period, where h is the bathymetry and g the gravitational acceleration.

Submarine landslide-generated tsunamis display distinct characteristics compared to earthquake-generated tsunamis (Trifunac & Todorovska 2002; Harbitz *et al.* 2006, 2014). Vertical displacements at the source can be larger in comparison to earthquake source, and lead to potentially higher amplitude waves (Okal & Synolakis 2003). Moreover, seismic rupture is most often considered effectively instantaneous, whereas landslide motion can last over several minutes to hours, leading to complex patterns of interactions between the different waves produced by the slide motion (Haugen *et al.* 2005; Harbitz *et al.* 2006; Ma *et al.* 2013; Løvholt *et al.* 2015). The pattern of landslide-generated tsunamis is more radial than in the case of earthquake sources, and displays different polarity properties. Because of their smaller source dimensions, landslide-generated tsunamis are more affected by frequency dispersion, affecting the tsunami celerity. These effects result in shorter wavelength and
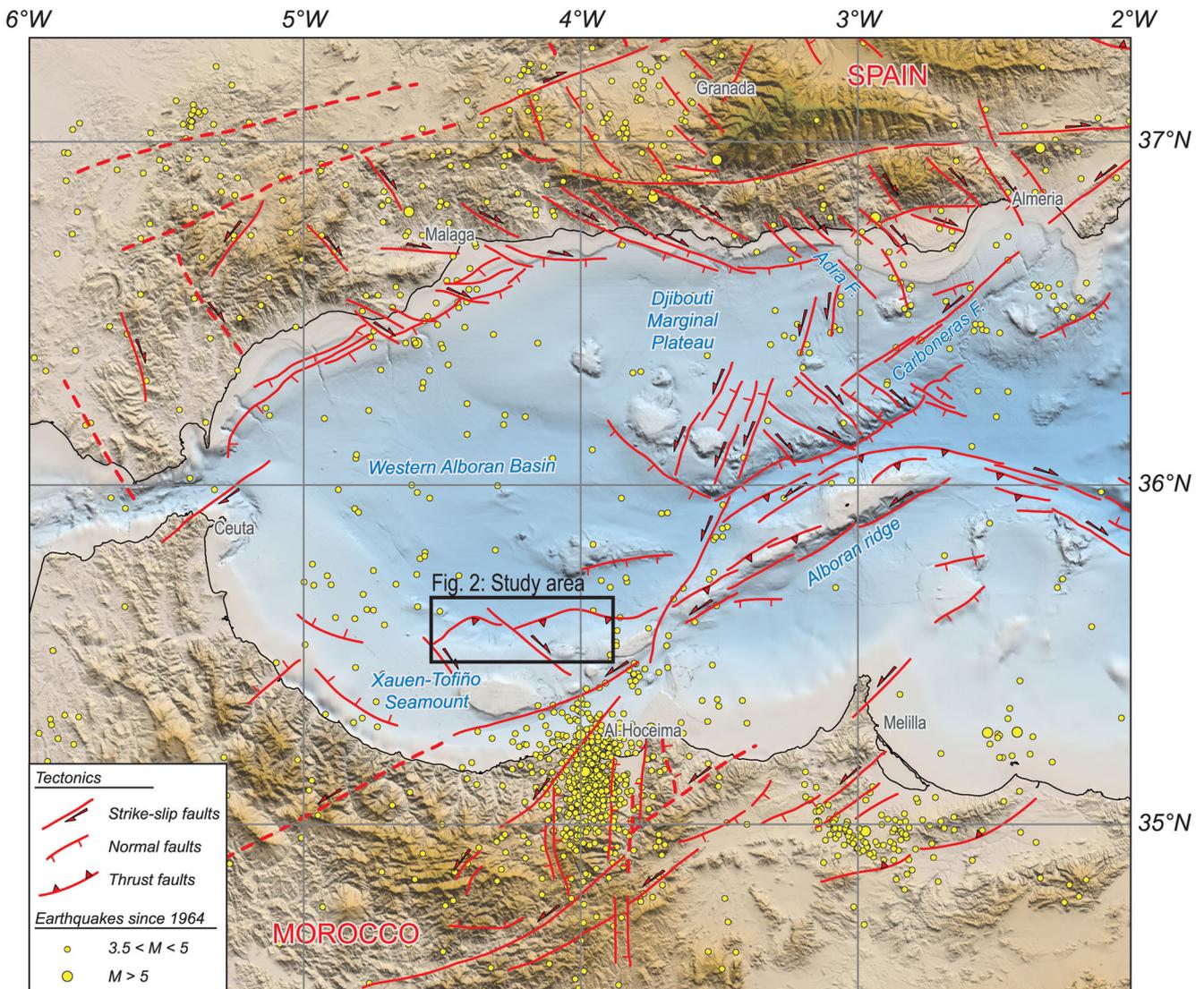
Figure 1. (a) Seismotectonic map of the Alboran Sea. Earthquakes since 1900 are from the Instituto Geogràfico Nacional catalogue (http://www.ign.es/ign/layoutIn/sismoFormularioCatalogo.do). (b) Cross-section of the Xauen–Tofiño banks, redrawn after Chalouan *et al*. (1997). P: Pliocene, M: Messinian unconformity and MM-T: Middle Miocene-Tortonian.

faster wave amplitude attenuation, and limit the far-field propagation of the tsunami. In places where submarine landslides occur along continental slopes, the distance to the coastline, and hence the propagation time, is often too short to allow the evacuation of coastal populations.

At the scale of the Western Mediterranean Sea, historical records and multibeam mapping revealed the distribution of some potentially tsunamigenic submarine landslides (Urgeles & Camerlenghi 2013). In 1979, a submarine landslide of about 0.01 km³ triggered a tsunami in the vicinity of Nice (SE France), producing waves on the order of 3 m in some areas (where water depths < 30 m, Ioualalen *et al*. 2010; Labbé *et al*. 2012). Submarine landslides are identified along the slope of the Ligurian margins (Migeon *et al*. 2011), the Gulf of Lions (Sultan *et al*. 2007) and the Eivissa Channel between the Iberian Peninsula and the Balearic Promontory (Camerlenghi *et al*. 2009; Berndt *et al*. 2012; Lafuerza *et al*. 2012; Vanneste *et al*. 2014). About 11 500 yr ago, the ~26 km³ BIG'95 landslide off the Ebro margin in Eastern Spain (Lastras *et al*. 2002; Canals *et al*. 2004) could have produced a tsunami with wave amplitude

potentially reaching 8 m in the vicinity of the Balearic Islands (Iglesias *et al*. 2012; Løvholt *et al*. 2014).

Although several submarine landslides have been identified in the Alboran Sea (Estrada *et al*. 1997; Martìnez-Garcìa *et al*. 2009; Casas *et al*. 2011; Alonso *et al*. 2012, 2014; Vázquez *et al*. 2013; Ercilla *et al*. 2015; Juan *et al*. 2016), it remains a place where their implications for tsunami hazard have not been fully investigated. Multibeam and echosounder data acquired during the SARAS cruise in 2012 reveal previously unrecognized complex submarine landslides in the southern Alboran Sea, where tectonic inversion formed the Xauen–Tofiño anticline system since the Late Miocene. There, submarine landslides rework the plastered contouritic drift, which drapes the Xauen–Tofiño anticline system (Figs 1 and 2). Here, we adopt a deterministic approach (Geist & Lynett 2014) based on the evaluation of maximum credible scenarios of tsunami generation over the semi-enclosed Alboran Basin, which encompasses the Moroccan coasts, the Alboran Island and the southern Iberian Peninsula coasts. In this study, the maximum scenarios are defined as the potential tsunamis that could be
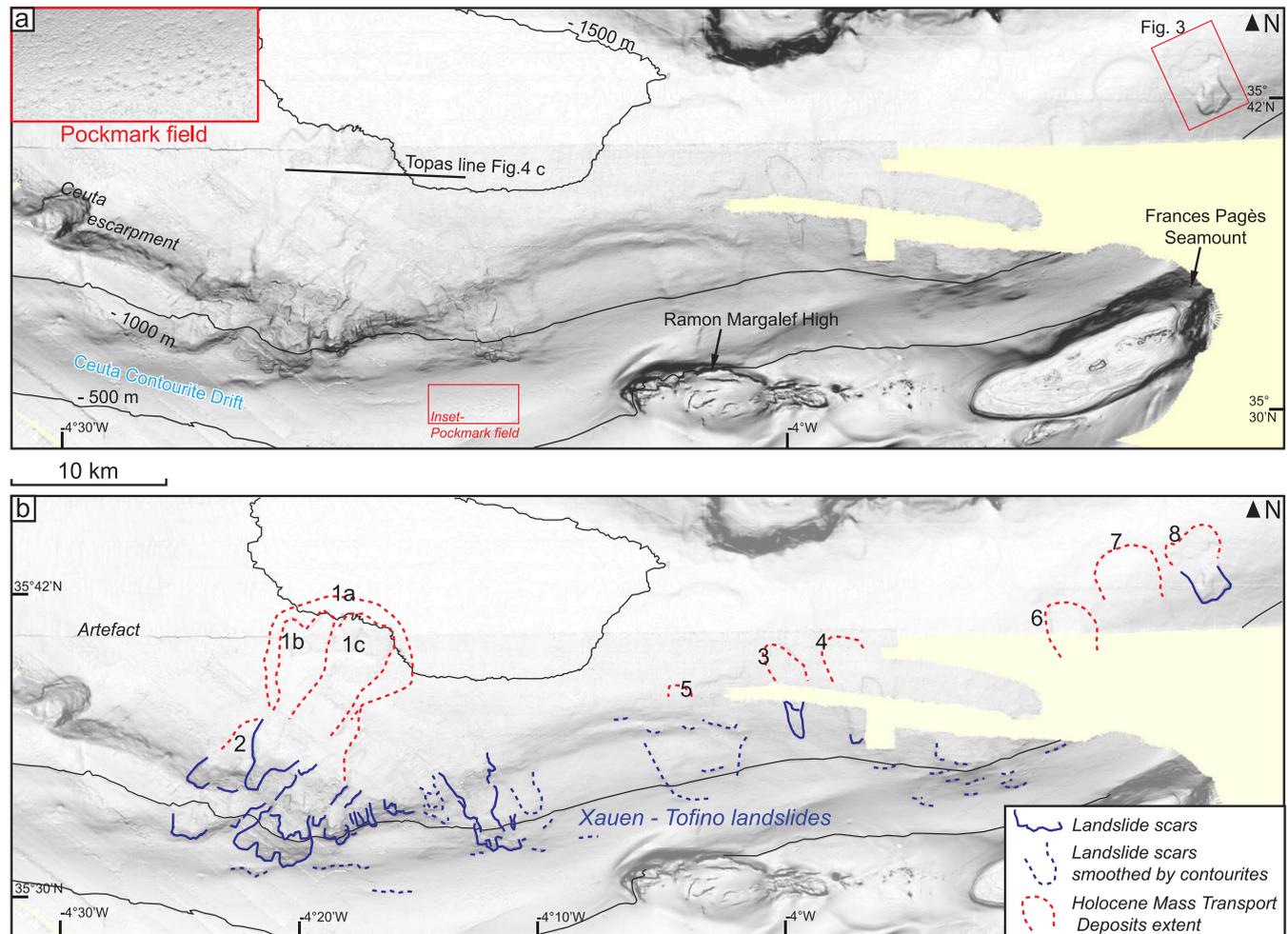
Figure 2. Shade relief map of the northern flank of the Xauen–Tofiño banks. (a) Uninterpreted map. Inset shows a close view of a pockmark field observed in the vicinity of the landslide scars. (b) Interpreted map, showing the distribution of recent scars, scars smoothed by the contouritic blanket and the extent of Holocene mass transport deposits. Contour lines at 500 m interval. See Fig. 1 for the location of the multibeam coverage.

generated by a landslide similar to the largest landslide observed on the Xauen–Tofiño banks. We consider a range of physical parameters for the sedimentary flow that reproduces, at the first order, the morphology of the slide deposits.

The first objective of this study is to provide a detailed morphologic description of submarine landslides observed along the northern flank of the Xauen–Tofiño banks with a particular emphasis over the estimation of the volume of sediments involved during the first stage of failure and the volume of the final mass transport deposit (MTD). The second objective is to evaluate the tsunamigenic potential of the most voluminous landslide by the mean of numerical modeling of tsunami generation and propagation.

This study stresses that such slides frequently encountered at the mid-slope of continental margins (e.g. the Vesterålen slides off Norway; L'Heureux et al. 2013) should not be neglected for tsunami hazard assessment, as they may locally represent a moderate threat for the nearby coasts.

2 REGIONAL SETTING

2.1 Geological background

The Alboran Sea is located between the Betic Cordillera in southern Iberian Peninsula, the Rif and Tell belts in Northern Africa,

the Gibraltar Strait to the West and the Algero-Balearic Basin to the east (Fig. 1). There, the Nubia–Eurasia plate boundary is expressed by a complex system of active conjugate strike-slip faults, referred as the Trans-Alboran Shear Zone (Fig. 1; Larouzière et al. 1988; El Mrabet 2005). The left-lateral strike-slip system runs from Almería in south-eastern Iberian Peninsula towards the Al Hoceima region, in Northern Morocco (d'Acremont et al. 2014; Lafosse et al. 2016; Fig. 1). The conjugate, right-lateral strike-slip system runs from northern Algeria towards Malaga in southern Iberian Peninsula (Fig. 1). The Alboran Sea displays conspicuous morphological features (Vázquez et al. 2015), such as the Djibouti-Motril Marginal Plateau (700–900 m deep) and the Alboran Ridge, locally emerged at the Alboran Island (Fig. 1). Several compressive structures are associated to the strike-slip boundary, including the ∼50-km-long Xauen–Tofiño anticline system at the western termination of the Alboran Ridge (Figs 1 and 2).

The physiography of the Alboran Basin results from a complex geological history occurring in the complex realm of convergence between Nubia and Eurasia (Bourgois et al. 1992; Woodside and Maldonado1992; Jolivet et al. 2009; Martìnez-Garcìa et al. 2013; Do Couto et al. 2014). The tectonic evolution of the Alboran Sea has been dominated by backarc extension related to the retreat of the western Mediterranean subduction zone during the Oligo-Miocene (Comas et al. 1999; Torne et al. 2000; Jolivet et al. 2009;

DoCouto *et al.* 2016, and references therein). As a result, the Alboran Basin is currently supported by a stretched metamorphic continental crust. Since Tortonian times (11.6–7.2 Ma), the retreat of the western Mediterranean subduction zone drives tectonic inversion (i.e. seafloor uplift) in the Alboran Basin (DoCouto *et al.* 2016), expressed by fold systems including the Xauen–Tofiño banks.

Sedimentary processes also played an important role in shaping the morphology of the Alboran Sea. Conspicuous contouritic drifts developed in relationship with the circulation of Mediterranean water masses merging into the Mediterranean Outflow Water at the Strait of Gibraltar (Ercilla *et al.* 2002, 2015; Somoza *et al.* 2012; Juan *et al.* 2016). Since the opening of the Gibraltar Strait 5.3 Ma and the end of erosive events related to the Messinian (Loget & Van den Driessche 2006; Bache *et al.* 2009; Garcia Castellanos *et al.* 2009; Estrada *et al.* 2011; Martìnez-Garcìa *et al.* 2013; Hernández-Molina *et al.* 2014; Roveri *et al.* 2014), up to 650-m-thick Ceuta contourite drift (Fig. 1) built-up synchronously with the growth of tectonic structures (Hernández-Molina *et al.* 2011; Somoza *et al.* 2012; Ercilla *et al.* 2015; Juan *et al.* 2016). According to available Ocean Drilling Program (ODP) wells, Pleistocene sediments mainly consist of fine-grained distal marls, silty clays and scarce interbedded sandstones (Alonso *et al.* 1999; Comas *et al.* 1999). The average sedimentation rate of the basin contourites around the study area is on the order of $\sim$190 m Ma^{-1} for the Pleistocene measured at ODP Site 979 (Alvarez-Marrón 1999), with higher sedimentation rates ranging between 250 and 320 m Ma^{-1} since 0.26 Ma (Martìnez-Garcìa *et al.* 2013).

2.2 Active tectonics and sources of tsunami hazard

Geodetic studies document a moderate, NW-SE to WNW-ESE convergence rate of 4–5 mm yr^{-1} between Eurasia and Nubia (Nocquet & Calais 2004; Fernández-Ibáñez *et al.* 2007; Serpelloni *et al.* 2007; Pérouse *et al.* 2010; Koulali *et al.* 2011). The convergence generates numerous seismic events (Macías *et al.* 2015), including strong earthquakes such as the M_w 6.0 earthquake in 1994 May 26 and the M_w 6.4 earthquake in 2004 February 24 in the area of Al Hoceima, Morocco (Bezzeghoud & Buforn 1999; Stich *et al.* 2005; Van der Woerd *et al.* 2014). The study area has been affected by a seismic crisis since the end of 2016 January, with more of 1500 events with magnitudes up to 6.1 (Galindo-Zaldívar *et al.* 2016). Offshore events as large as $M_w \sim$ 7.1 have been recorded along the Trans-Alboran Shear Zone (according to the compilation of Alvarez-Gomez *et al.* 2011a,b). In the historic record, one of the most notable earthquake (M_w 6.1) was triggered at the Adra Fault in South East Spain in 1910 (Gràcia *et al.* 2012).

Only a modest tsunami hazard is expected from earthquakes, because of the dominant strike-slip component of the fault systems (Fig. 1). Estimated maximum tsunami elevations for seismic sources reaches 0.5 m at the coastline between Malaga and Almería (for water depths <80 m, Alvarez-Gomez *et al.* 2011a,b). An exception is the fault system crossing the Alboran Ridge (Fig. 1), which may be capable of generating tsunamis with wave heights up to 1.5 m at the receiving shores (for water depths <80 m) in Spain and Morocco according to numerical models (Alvarez-Gomez *et al.* 2011a,b). The seismic activity of the North Algerian Fold and Thrust Belt constitutes a moderate tsunami hazard at the entrance of the Alboran Sea (Alvarez-Gomez *et al.* 2011a,b), with maximal water heights on the order of 0.3–0.4 m measured at tide gauges between Cartagena and Alicante (South Eastern Spain) for the 1980 El-Asnam earthquake (Roger *et al.* 2011). The record of historical

tsunamis documents several events in this area in AD 1365, 1773 and 1856 (Roger & Hébert 2008; Papadopoulos *et al.* 2014).

Potentially tsunamigenic landslides in the Alboran Sea have been identified at the southern Alboran Ridge (Al-Borani landslide, Macías *et al.* 2015), along the northern Alboran continental slope (Baraza Slide, Casas *et al.* 2011) and northeastern seamounts (Alonso *et al.* 2014). The Al-Borani landslide may be a potential tsunami source with maximal amplitude of the wave on the order of 1 m at the Moroccan coastline (i.e. for water depths < 80 m), if the scar is considered as a result of a single landslide (Macías *et al.* 2015). Another suspected source of landslide tsunami is related to the Carboneras Fault system in southeastern Iberian Peninsula (Fig. 1). The 1522 Almería earthquake may have triggered a submarine landslide along its offshore segment, which probably contributed to the generation of a tsunami (with runup up to 1–3 m) well recorded in coastal sediments (Reicherter & Becker-Heidmann 2009). Traces of this hypothetic slide remain to be discovered offshore Almería.

2.3 Slope instability: pre-conditioning factors and triggering processes

Several processes observed in the Alboran Sea may influence the evolution of slope stability and control the distribution of submarine landslides (Baraza & Ercilla 1994; Casas *et al.* 2011; Martínez-Garcìa *et al.* 2013; Alonso *et al.* 2014). First, the observation of the local collapse of the Ceuta Drift (Somoza *et al.* 2012) confirms high sedimentation rates (>100 m Myr^{-1}) within contourite drift as a pre-conditioning factor of slope instability (Rebesco *et al.* 2014). Failure triggering by sediment accumulation rates alone is however unlikely according to theoretical grounds (Viesca & Rice 2012; Urlaub *et al.* 2015). Fluid circulation (gas and liquid mud) observed within the contouritic drift (inset in Fig. 2; Pérez-Belzuz *et al.* 1997; Blinova *et al.* 2011; Somoza *et al.* 2012) may also promote slope instability through pore pressure buildup, as observed elsewhere in the Mediterranean Sea (Lafuerza *et al.* 2012; Urgeles & Camerlenghi 2013) or, for instance and at a larger scale, the Storegga slide off Norway (Mienert & Posewang 1999; Bryn *et al.* 2005; Bünz *et al.* 2005; Kvalstad *et al.* 2005). Earthquake shaking related to the activity of the Trans-Alboran Shear Zone may ultimately trigger slope destabilization, through the generation of horizontal and vertical ground accelerations induced by seismic waves and the simultaneous increase of pore pressure (Hampton *et al.* 1996).

3 MATERIAL AND METHODS

3.1 Bathymetry and echosounder profiles

The swath bathymetry was acquired during the SARAS cruise (2012) over the Xauen–Tofiño banks with a Kongsberg multibeam echosounder, which operates at sonar frequencies in the 70–100 kHz range. The grid cell size is 15 m, while its vertical resolution is around 1–2.5 m for a water depth below 500 m. In addition, very high resolution seismic profiles were acquired with a Kongsberg parametric subbottom profiler TOPAS PS18. The TOPAS system transmits a modulated frequency sweep between 0.5 and 6 kHz. The penetration of the acoustic signal achieved with the TOPAS system varies between 0 and 200 m at full oceanic depths and the resolution is around 10 cm.

To complete the new swath bathymetric coverage presented in this study, several multibeam bathymetry data sets obtained during previous cruises were merged for tsunami modeling at the scale of the Alboran Sea.
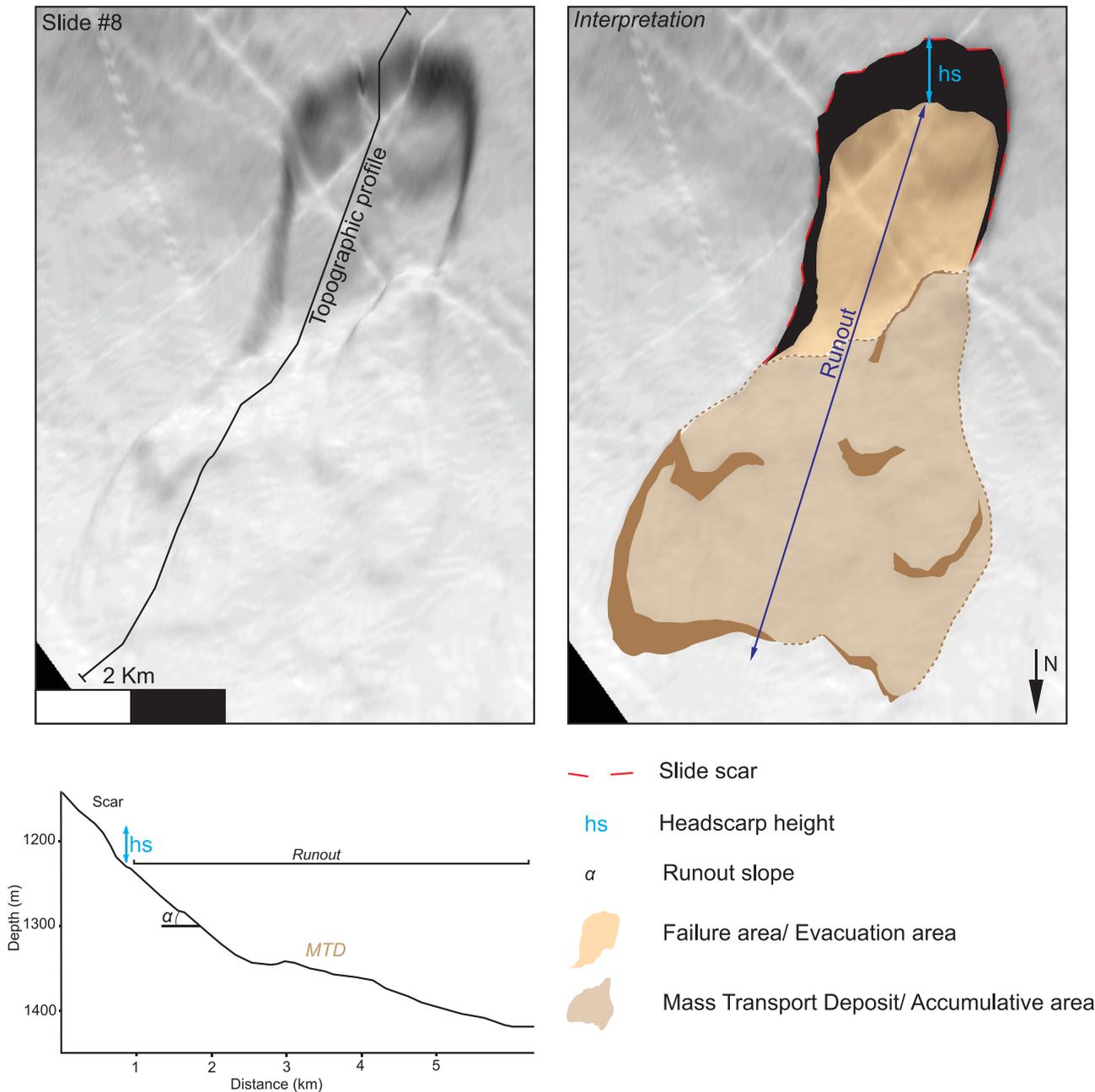
Figure 3. Shade relief map of slide 8 (see Fig. 2 for location), and related interpretation, highlighting the different morphometric parameters used in this study.

3.2 Morphological analysis of submarine landslides

Multibeam bathymetry and subbottom profiler are powerful tools to map the distribution of submarine landslides, the morphology of their scars and the extent of their deposits at the scale of a continental margin (Mc Adoo *et al.* 2000; Chaytor *et al.* 2009; Twichell *et al.* 2009; Tappin 2010; ten Brink *et al.* 2014). Nomenclatures of submarine landslides deposits are mainly based on detailed core analysis, where the large variety of granulometric patterns reflects the behaviour of the sedimentary flow (Mulder & Cochonat 1996; Mulder & Alexander 2002). Multibeam bathymetry and subbottom profiles do not allow the application of such detailed nomenclatures, but provide some of the first-order constraints on the morphological characteristics of the mass movements necessary for tsunami modeling.

A set of morphological parameters has been systematically measured to characterize the landslide scars and the related MTD along the Xauen–Tofiño banks (Fig. 3). The headscarp delineates the failed area, and its height provides an indication on the depth of the failure plane (Fig. 3). The geometry of the scar allows to delineate the excavation formed by the landslide (failure area) and to estimate its volume at the inception of the failure. The volume of sediments mobilized at the incipient stage of failure is estimated following the method described in ten Brink *et al.* (2006). It consists in filling-in the failed area according to the adjacent scar height. The difference between the filled-in grid and the grid displaying the slide scars gives the failed volume. In detail, we identify several areas of overlapping subparallel scars at headwall escarpments, referred to as 'Headwall collapse areas' (Figs 4a and b), where the cohesion of the sediment remains intact in spite of internal deformation
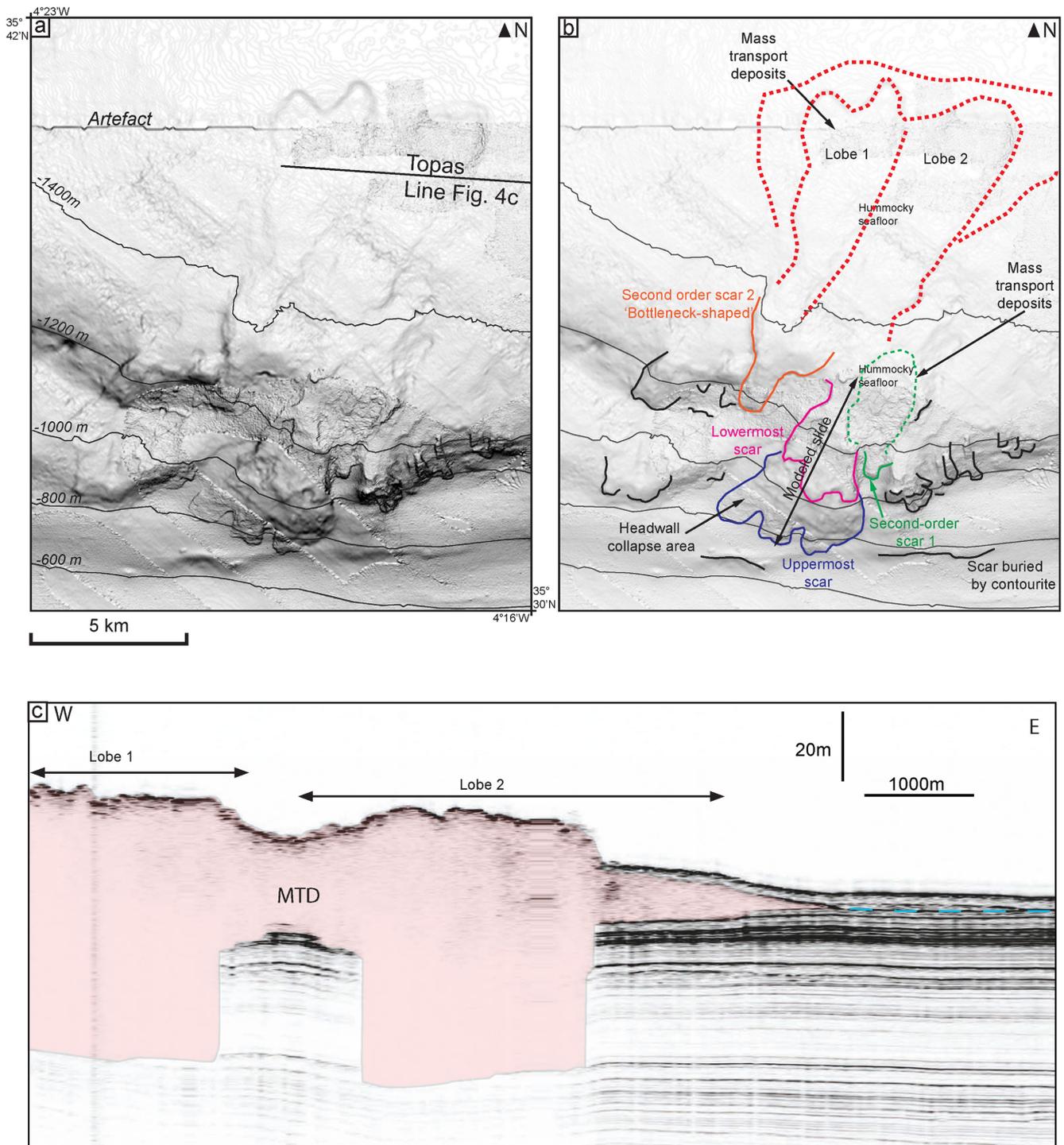
Figure 4. Detailed morphology of the modeled landslide (slide 1). (a) Uninterpreted shade relief map of the landslide. (b) Interpreted shade relief map, highlighting several imbricated scars, and lobe-shaped MTDs. (c) TOPAS profile crossing the MTD 1. See Table 2 for morphometric details for slide 1.

(creeping or shallow faulting above the failure plane; e.g. Kvalstad *et al.* 2005; Micaleff *et al.* 2007). Sediments in headwall collapse areas are displaced along the failure plane at the origin of the landslides, but did not evolve into a sedimentary flow. Depending on the study area, headwall collapse features can be the result of retrogressive (Piper *et al.* 1999; Rodriguez *et al.* 2012) or progressive (Omeru & Carthwight 2015) erosion. Because these parts of the failed area do not directly contribute to the sedimentary flow during the slide, they are excluded from volume estimation of the initial

failed sedimentary mass. However, they give an indication of the likely failure area for the computation of the worst case scenario of a sedimentary failure.

The extent of MTDs are mapped from their lobe shape, their hummocky facies and the extent of blocks recognized on multibeam data, and their chaotic to transparent facies on echosounder profiles (Fig. 4c). The distance between the head of the scar and the toe of the lobe defines the runout of the slide. Where most of the failed mass has been evacuated outside of the area enclosed by the scar, the

failure is described as 'disintegrative' (following the terminology of Mc Adoo *et al.* 2000). A disintegrative pattern results from the loss of cohesion of the failed sedimentary mass either during failure, or by incorporating fluids during its downslope movement. Base and top of the MTD are picked on echosounder profiles to define their thickness, and interpolated according to their extent on the high-resolution bathymetry in areas where profiles are missing. The detailed mapping allows the estimation of the volume of the MTD, taking into account the amount of sediment incorporated to the slide during its motion. *P*-wave velocities on the order of 1550 m s^{-1} (measured in nearby shallow sediments; Martìnez-Garcìa *et al.* 2013) are used to convert two way traveltime to metres.

3.3 Tsunamis calculations

3.3.1 Slide modeling: physical background and limits

The code has been described in details and successfully tested for the 1998 Papua New Guinea event (Heinrich *et al.* 2001) and the 1979 Nice event (Labbé *et al.* 2012). The model is based on the shallow-water assumption, justified by the slide thickness being much smaller than its length and width (Heinrich *et al.* 2001). Two approaches are commonly adopted for landslide modeling. The approach commonly used in previous studies of submarine hazard in the Mediterranean Sea (Iglesias *et al.* 2012; Løvholt *et al.* 2014) assimilates the slide to a viscous flow with a Bingham rheology, where the flow is divided into a bottom layer submitted to shear, and a top plug layer with an uniform velocity profile over its thickness (Jiang & Leblond 1992). However, in the case of the Xauen–Tofiño landslides, the Bingham flow simulations carried for a reasonable range of dynamic viscosities (25–500 m s^{-2}) failed to reproduce the first-order morphology of the slide deposits, and lead to excessive runout and volume values compared to the observations. Simulations assimilating the slide to a granular flow (second approach, Savage & Hutter 1989) are more consistent with the observations, which are consistent with a removed material dominantly composed of silt, as suggested by some drilling sites analysis in various places of the Alboran Sea (Skilbeck & Tribble 1999).

Modeling a granular flow with a short runout distance (i.e.< 30 km) assumes that the landslide breaks into fragments in the early stages of collapse and that it may be assimilated to a fluid-like flow of cohesionless granular material (Savage & Hutter 1989). The mechanism initiating the landslide is not investigated in this study and it is assumed that the whole mass suddenly loses its equilibrium and begins to flow downslope under gravity forces. Deformation occurring within the flow in the earliest stages of collapse and potential effects of retrogressive failure on tsunami generation (Haugen *et al.* 2005) are therefore not considered. The model of landslide propagation is based on the shallow-water assumption, with slide thickness much smaller than its length and width. The shallow-water equations are solved in two spatial horizontal propagation directions (*x* and *y*) and one temporal direction (*t*).

Although large deformations throughout the thickness of the flow are inevitable (ten Brink *et al.* 2014) and may have important effects on the evolution of the tsunami wave (Ma *et al.* 2013), the shallow-water approximation implies that the mechanical behaviour within the flow is simplified in the model of landslide propagation: most fragment collisions and deformations are assumed to be concentrated in the boundary layer near the bed surface (Savage & Hutter 1989). The model of Savage & Hutter (1989) does not take into account the added mass effect (ambient water or eroded sediments during the slide motion) that can significantly reduce the accelera-

tion of the slide (Løvholt *et al.* 2015), and therefore, the amplitude of the generated wave.

Energy dissipation within the flow is then neglected compared to that lost through the boundary layer, and the slope-parallel velocity is assumed to be constant over the flow thickness. A Coulomb-type friction law with a constant friction angle, independent of the shear rate, describes basal friction. This law assumes a constant ratio of the shear stress to the normal stress at the base and involves a dynamic friction angle φ between the rough bed and the mass. When the flow is close to rest, the fluid velocity is set to 0 as soon as the Coulomb force is larger than the algebraic sum of the forces due to gravity and height gradient. In submarine environments, only low values of the friction angle (<15°) are appropriate to reproduce the mobility of real submarine landslides. Submarine landslides can even occur on low angle (<2°) slopes with low sedimentation rates (0.15 m kyr^{-1}), due to various processes (fluid circulation and diagenetic processes) able to increase pore pressure in the sediment column and trigger slope failure (Urlaub *et al.* 2015). Therefore, we perform simulations only for friction angles ranging between 1° and 15° to simulate the landslides observed at the Xauen–Tofiño banks.

The resulting equations of mass and momentum conservation, written in a coordinate system linked to the topography, read:

$$\frac{\partial h}{\partial t} + \frac{\partial}{\partial x}(h\boldsymbol{u}) + \frac{\partial}{\partial y}(hv) = e_w \, \|u + v\|$$

$$\frac{\partial}{\partial t}(h\boldsymbol{u}) + \frac{\partial}{\partial x}(h\boldsymbol{u}.\boldsymbol{u}) + \frac{\partial}{\partial y}(h\boldsymbol{u}.v)$$

$$= -\frac{1}{2}\kappa \frac{\partial}{\partial x}(gh\cos\theta) + \kappa gh\sin\theta_x + \boldsymbol{F}u$$

$$\frac{\partial}{\partial t}(hv) + \frac{\partial}{\partial x}(hv.\boldsymbol{u}) + \frac{\partial}{\partial y}(hv.v)$$

$$= -\frac{1}{2}\kappa \frac{\partial}{\partial y}(gh\cos\theta) + \kappa gh\sin\theta_y + \boldsymbol{F}v$$

where $\kappa = 1 - \rho_w/\rho_s$, $\boldsymbol{u} = (u,v)$ is the depth-averaged velocity vector parallel to the bed, h is the slide thickness perpendicular to the slope, $\rho_w = 1000$ kg m^{-3} is the water density and $\rho_s = 2000$ kg m^{-3} is the sediment density, $\theta(x,y)$ is the local steepest slope angle, θ_x and θ_y are the slope angles along the *x*- and *y*-axes, respectively. $\boldsymbol{F} = -\kappa \, gh \, \cos\theta \, \tan\varphi \, \boldsymbol{u}/\|\boldsymbol{u}\|$ is the Coulomb friction force and φ is the basal friction angle. The coefficient of water entrainment e_w is considered as a constant taken in the 0–10^{-3} range, (which is two orders less than the values used for turbidity currents; Fukushima *et al.* 1985; Kostic & Parker 2006; Seiqueiros *et al.* 2009). It corresponds to the dilution of the sedimentary mass by water incorporation at the interface between the slide and the water. This coefficient of water entrainment is used to increase the volume of the slide during its downslope motion, but it does not have any effect on the acceleration pattern of the slide. Our landslide simulations are unable to reproduce the erosion of the seafloor during the slide motion (evidenced on Fig. 4c), which contributes to the increase of slide volume, and may also affect its velocity.

The most important limit in modeling past submarine landslides is the impossibility to provide precise constraints on the pattern of velocity and acceleration of the slide from multibeam, seismic or core data (Harbitz *et al.* 2006; Ma *et al.* 2013; Løvholt *et al.* 2015). We therefore consider scenarios where slide velocities are compatible with the few constraints available from submarine cable breaks recorded in the 20th/21st centuries (i.e. with mean velocity <20 m s^{-1}; Heezen & Ewing 1952; Mulder *et al.* 1997; Fine *et al.* 2005; Carter *et al.* 2014).

Table 1. Morphometric parameters of submarine landslides (scars and MTDs) along the Xauen and Tofiño Bank. See Fig. 2 for the location of MTDs.

MTD number	Surface of the MTD (km^2) (± 0.1 km^2)	Volume of the MTD (km^3) (± 0.1 km^3)	Volume of sediments at the initial stage of failure (km^3) (± 0.1 km^3)	Runout (km) (± 0.1 km)	Slope at the scar (°) (± 0.1°)
1a	90.2	2.2	0.5	19.9	12
1b	20.6	1.2			
1c	21.9	1.2			
2	8.4	0.1		9	9
3	5.9	0.1	0.01	7.1	6
4	1.8	0.03		5	11
5	0.6	0.01		2.6	5
6	6.6	0.2		5.9	5
7	9	0.3		9.5	7
8	8.7	0.2	0.06	4.8	9

3.3.2 Tsunami modeling

Simulations of the tsunami waves are also based on the shallow-water approximation (the length of water waves is larger than the water depth), which deals with the full interaction of landslide and water, including the deformation of the sediment body. Equations governing the landslide and the tsunami propagation are similar and are thus solved using the same Godunov-type scheme, extended to second order by using the concept of Vanleer (Alcrudo & Garcia-Navarro 1993; Mangeney *et al.* 2000). The time history of sea bottom deformation resulting from the landslide is introduced as a known forcing term $(\cos\theta)^{-1}\,\partial h/\partial t$ in the mass conservation equation of the tsunami model.

4 THE SUBMARINE LANDSLIDES ALONG THE XAUEN–TOFINO BANKS

4.1 General morphological characteristics

The northern flank of the Xauen–Tofiño banks shows evidence for eight Holocene landslides, expressed by scars at the headwall domain and debris flow deposits at the toe domain (Fig. 2 and Table 1). Where seafloor signatures of MTDs are fresh, remaining uncovered by other deposits, MTDs are considered as Holocene in age. All MTDs covered by various thicknesses of sediments are considered as pre-Holocene and not considered in this study.

The landslide scars are observed on the slope ranges between 6° and 8°, with the major slope break around 1000 m of water depth. The head of the scars are clustered at the mid-slope, around water depths of 700–800 m and 1000–1100 m, whereas the fronts of the deposits lie around 1400–1500 m. Runout values range between ∼2 and 20 km. All the landslides are disintegrative. Landslides observed in the eastern area (slides 3–8; Fig. 2) display well-defined lobe deposits and are associated with simple arcuate scars. Landslides observed in the west (slides 1 and 2; Fig. 2) display more complicated morphologies with several imbricated and uneven scars (Fig. 2). Among the eight Holocene MTDs, only one reaches a volume of more than 2 km^3 (Table 1). The trace of older landslides (i.e. partially smoothed by the contouritic blanket) is observed along the strike of the Xauen–Tofiño banks (Fig. 2).

4.2 Detailed morphology of the most voluminous landslide

A complicated landslide complex is identified in the western study area (slide 1; Figs 2 and 4). The main scar complex is composed of two main imbricated scars (1b and 1c), indicating a multifailure event or a poly-phased one (Figs 4a and b). The uppermost scar (750–800 m water depth) is composed of three main merged concave scars, delineating slightly deformed to hummocky areas interpreted as headwall collapse features (Figs 4a and b). The headwall collapse domain spreads over ∼8.7 km^2 down to the lowermost scar. The lowermost main scar (in 1000–1100 m water depth) is also composed of three main merged individual scars (Fig. 4b). The lowermost scar encloses an >7 km^2 area of smooth seafloor. Adjacent hummocky deposits coming from a second-order failure located on the eastern side of the lowermost scar cover an area of ∼7 km^2 (Fig. 4). The initial failed area associated to the lowermost scar was therefore on the order of ∼14 km^2. The difference between the present-day bathymetry and the reconstructed seafloor prior to the landslide gives a volume of sediments removed during the first stage of failure of ∼0.5 km^3. An additional scar complex, located in between 1120 and 1400 m water depths on the western side of the main scar complex, displays a bottleneck shape, with the scar narrowing upward (Figs 4a and b). The likely failure area is estimated to around 9.9 km^2, and the failed mass was on the order of 0.12–0.2 km^3.

The MTDs mapped in front of these scar complexes spread over 90 km^2 and include two lobes (lobes 1 and 2) well identified in the bathymetry data (Fig. 4a). The TOPAS profile shows the lobes results from two distinct U-shaped pathways of the slide (Fig. 4c). MTDs filled-in the evacuation pathways and covered them after overspilling. The lack of a full coverage of the MTD by TOPAS profiles induces strong uncertainties in volume estimates. The volume of MTD trapped in the evacuation pathways and forming the lobes is on the order of 3.6–5.6 km^3, if considered as the result of a single failure event. The maximum volume of mobilized sediments from the morphology of the scars is only 0.7 km^3 (considering all the scars in front of the MTD correspond to a single destabilization event). This discrepancy indicates a significant growth of the volume (increase by ∼5–8 times) of the slide during its motion.

5 TSUNAMI MODELING RESULTS

The morphological analysis documents the presence of landslide whose volumes range between the volume of the slide responsible of the 1979 tsunami at Nice (0.01 km^3; Labbé *et al.* 2012) and the volume of the slide that triggered the tsunami of Papua-New Guinea in 1998 (∼3.8 km^3; Heinrich *et al.* 2001), which justifies the analysis of their tsunamigenic potential. We first determinate the physical parameters able to reproduce a slide similar to the slide composed

Table 2. Morphometric parameters of landslide 1 scars.

Landslide 1 scars	Water depth (m)	Scar length (km) (±0.1 km)	Failure area (km²) (±0.1 km²)	Morphology
Uppermost scar	750–800	13	8.7	Three imbricated scars delineating a headwall collapse area
Lowermost scar	1000–1100	9	14	Three imbricated scars
Second-order scar 1	1050–1100	9.2	7	Single arcuate scar
Second-order scar 2	1120–1400	1.6	9.9	'Bottleneck-shaped' scar

of the imbricated scars between 4°23′W and 4°19′W (slide 1; Fig. 4), and then simulate the tsunami that would be triggered by this slide. All the simulations performed for the other Xauen–Tofiño landslides show that there were unable to generate significant tsunami (i.e. with elevation at the coastline> 10 cm) in a range of reasonable flow parameters. In agreement with observations, we consider a scenario where the landslide is triggered as a single event, mobilizing 0.5 km³ of sediments (headwall collapse areas are incorporated in the initial volume, which constitutes a maximizing case). Some tests where several smaller landslides (like slides 3–8; Fig. 2) are triggered at the same time as the 0.5 km³ slide along the Xauen–Tofiño banks were also performed. The triggering of several smaller coeval slides does not produce remarkable interactions between waves and does not affect the propagation of the tsunami triggered by the most voluminous slide (0.5 km³) in a significant way, compared to the simulations where only the 0.5 km³ slide is triggered.

Granular flows commonly occur for basal friction angles φ ranging between 2° and 15°. However, for the case study of the slide 1 (Fig. 4), the range of reasonable values of the basal friction angle φ obtained after parametric tests is quite narrow, with $3.2° < \varphi < 3.5°$. When $\varphi > 3.5°$, the slide is too slow and the runout too short compared to the observations, which does not produce significant tsunami. Conversely, when $\varphi < 3.2°$, the velocity of the slide and its runout are too important and not consistent with the observations. For all the selected simulations, the maximum slide velocity does not exceed 30 m s^{-1}. The initial acceleration of the slide ranges between 0.5 and 0.6 m s^{-2} (considering an added mass coefficient of 1.2 would reduce the initial acceleration by $\sim 10^{-2}$ m s^{-2}). The peak of velocity at 30 m s^{-1} is reached about 3–4 min after slide inception, which corresponds to the time before the front of the slide reaches the break of slope at -1400 m, where MTDs start to be observed. Then the slide slows down and moves at a mean velocity of 15–20 m s^{-1}, while its volume starts to increase above 0.8 km³. This range of velocities is roughly similar to the velocity needed to reproduce the slide at the origin of the 1998 Papua-Guinea tsunami (Tappin *et al.* 2008). The increase of volume of the flow is simulated by using coefficient of water entrainment e_w of $\sim 10^{-3}$, producing a 3–5 times increase of the volume of the slide during the downslope motion in agreement with the observations. The simulations produce volumes of MTD ranging between 1.7 and 2.6 km³, which is compatible with the lower estimates from the multibeam and the TOPAS profile (on the order of 2.2–4.7 km³). The modeled volumes are lower estimates of the observed volume of the MTD, but are in the upper bounds of the distribution of the calculated volumes for the most recent MTDs.

All runs were performed with 200 m grid spacing, and simulate the propagation of the tsunami over 30 min after the slide initiation. The reported surface elevation of the tsunami at the coastline actually correspond to the height at a few kilometres from the coasts, as runup values cannot be properly modeled in the lack of detailed grids at the shore.

All simulations produce the same pattern of propagation, typical of landslide-generated tsunami (Ward 2001; Mohammed & Fritz 2012; Ma *et al.* 2013). The incipient radiated wave has two peaks and one trough at the source location (Fig. 5). The water ahead of the front face of the slide (i.e. the outgoing wave) is pushed away, creating a leading positive wave in the slide direction (i.e. towards southern Iberian Peninsula). The trough following the crest is simultaneously created by the slide excavation, and is followed by a large second positive peak created by the infilling of the trough. In contrast, the front of the backgoing waveforms a trough propagating towards Morocco, followed by a second positive wave (Fig. 4).

The best-fitting simulation (i.e. the one reproducing the slide deposits the most accurately) is obtained when considering an initial failed volume of 0.5 km³, a basal friction angle $\varphi = 3.2°$, and a water entrainment coefficient $e_w = 10^{-3}$, which results in an MTD of ~ 1.7 km³. At the source location, the elevation of the outgoing wave reaches 1 m, but is reduced after ~ 5 min of propagation (Fig. 5). The outgoing wave (i.e. in the same direction as the slide) reaches the coast of the southern Iberian Peninsula ~ 23 min after slide initiation (Fig. 5), the highest computed tsunami wave being on the order of ~ 20 cm all along the coastline. A minor amplification of the wave occurs at the edge of the Djibouti plateau and along the Alboran Ridge (Fig. 1). The second, positive peak of the backgoing wave (i.e. in the opposite direction of the slide) is amplified up to 40-cm by the 100-m-deep Xauen bank, and up to 0.9–1 m (where water depths <5 m) at the coastline of Morocco in front of the source, only after 13 min of propagation (Figs 5 and 6). In details, the main shoaling between El Jebha and Al Hoceima occurs between 16 and 20 min after the triggering of the slide (Fig. 6). The leading wave reaches the cape of Al Hoceima at 16 min, then the shoaling occurs when the wave enters the bay. The subsequent wave trains are amplified at the Xauen bank (see the configuration at 25 min; Fig. 6), but do not lead to major waves at the coastline. The tsunami reaches the coastline between Al Hoceima and Melilla >30 min after slide inception, but does not produce significant waves there (Fig. 6). Fig. 7 shows the map of the maximal elevation reached by the simulated tsunami, and highlights the fact that only El Jebha and Al Hoceima are affected by tsunami >0.5 m.

Considering an initial failed volume of 0.5 km³, a basal friction angle $\varphi = 3.5°$, and a water entrainment coefficient $e_w = 2 \times 10^{-3}$, results in an MTD of ~ 2.6 km³, which defines the maximal scenario. The computed wave shows the same pattern of propagation than the minimal scenario, with a similar maximal elevation of the positive backgoing wave at the Moroccan coastline (in front of the source) at 1 m. In spite of a more important volume, the distance between the source and the coastline is long enough to attenuate the tsunami wave. A moderate change in the volume of the failed mass (less than 1 km³) does not affect significantly the surface elevation of the tsunami at the coastline.

More generally, all the simulations performed for basal friction angles $3.2° < \varphi < 3.5°$ and e_w on the order of $\sim 10^{-3}$, despite
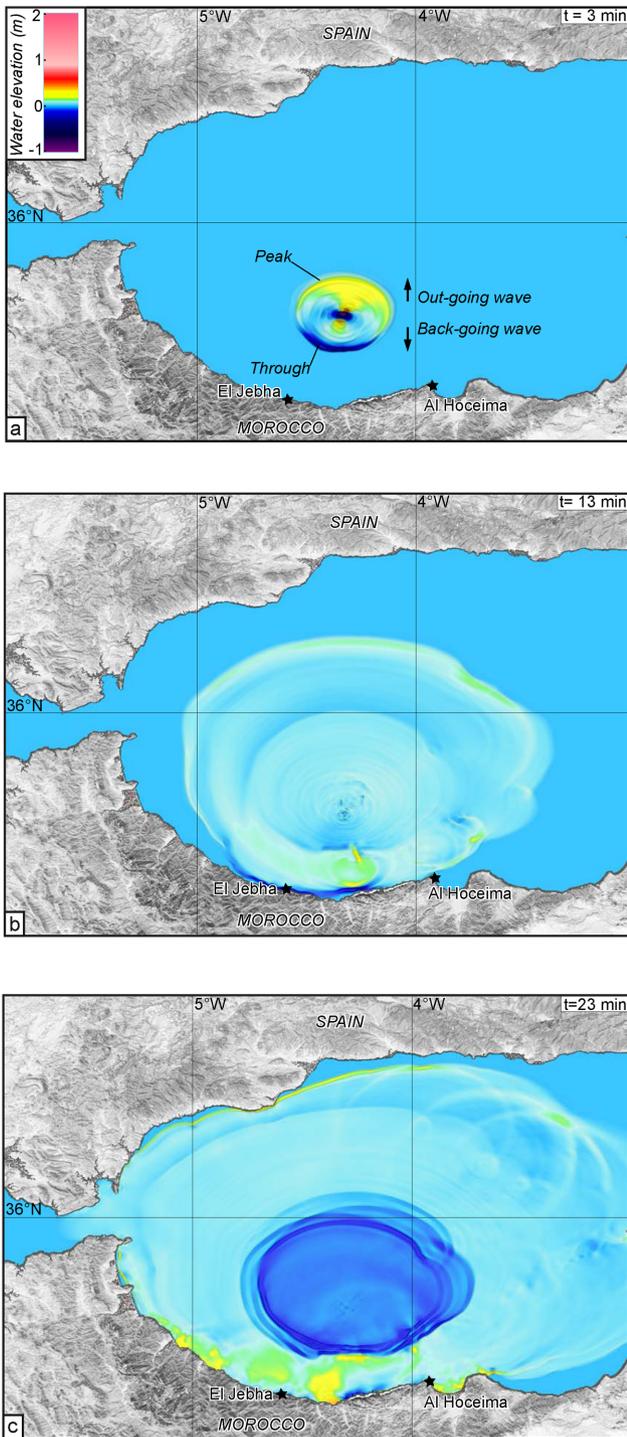
Figure 5. Propagation of the tsunami simulated for a landslide with an initial volume of 0.5 km^3, a basal friction angle $\varphi = 3.5°$ and a water entrainment coefficient $e_w = 2 \times 10^{-3}$. Snapshots after (a) 3 min, (b) 13 min and (c) 23 min of propagation.

producing different MTD volumes (about 1 km^3 of difference), produce the same tsunami elevation pattern at the coastline. Processes of attenuation between the source and the coastline are efficient enough to smooth the potential effect of a moderate increase in the slide volume over wave elevation at the coastline.

Fig. 8 shows a comparison between the modeled and observed extent of the slide and the related MTD (in the case of our maximizing scenario, i.e. producing a volume of 2.6 km^3). The model strikingly

reproduces the observed runout of the slide, and roughly reproduces the two-lobe shape of the MTD (Fig. 8). The maximal thickness of the computed slide (on the order of 40–50 m; Fig. 8) is compatible with the estimates from the TOPAS profile (Fig. 4). However, the computed thickness is underestimated in the distal part of the slide (10–20 m versus 40 m on the TOPAS profile). We were unable to model an increase of the thickness of the distal part of the slide without unrealistically increase the runout, which is probably due to the fact that our simulations does not take into account erosion. The extent of the modeled deposits is wider than what observed (Fig. 8). The evacuation pathways observed on the TOPAS profile (Fig. 4) may focus the flow in a preferential direction in the real case, resulting in locally thicker deposits than in the modeled case. Our simulations do not allow such accuracy in the modeling of the flow. The basal drag due to the erosion of the seafloor by the slide (Fig. 4c) may reduce its velocity, and therefore the tsunami waves generated at the end of the slide motion. However, the tsunami waves generated at this point are minor (<10 cm; Fig. 5) and their effect on the evolution of the tsunami can be neglected.

6 DISCUSSION AND CONCLUSIONS

Numerical results show that a landslide event similar to slide 1 (Fig. 2) between the longitude of 4°30′W–4°40′W along the northern flank of the Xauen–Tofiño banks can produce a tsunami with an elevation on the order of 1 m at the Moroccan coastline (Figs 5–7). One of the most threatened area is the coast near the city of Al Hoceima (400 000 inhabitants for the city and its suburbs, with the second largest harbour of this part of the Alboran Sea), which can be impacted by a tsunami wave of ∼0.5 m at the coastline (Figs 5–7). The highest (∼1 m) computed wave is close to the city of El Jebha (3000 inhabitants; Figs 5–7). The impact of the potential tsunami for the Spanish coast of the southern Iberian Peninsula is expected to be minor (Figs 5–7). The most dangerous characteristic of the tsunami potentially generated by the Xauen–Tofiño landslides is the short propagation time to the Moroccan coastline, on the order of 13 min. This short propagation time makes difficult the organization of alert systems based on detection of the tsunami, warning and evacuation of the population close to the shore. According to the most credible simulation, the impact of a tsunami from the Xauen–Tofiño landslides may be similar to the one of the tsunami simulated from the Al-Borani landslide along the Alboran Ridge, east of 3°W (Macías *et al.* 2015). The simulations also highlight tsunami elevation at the Moroccan coastline potentially equal to or locally higher than the wave expected for earthquake sources (6.7 < M_w < 7.3) at the Alboran Ridge (Alvarez-Gomez *et al.* 2011a,b).

The tsunami simulations have some limits. The first one is the lack of high-resolution bathymetry along the coast, or for instance of the harbour of Al Hoceima. It remains unknown if local bathymetric features or harbours would result in further amplification or dispersion of the tsunami wave. Even if the resolution of the grid at the coast does not allow accurate computation of the flooding, runup values are often more important than the water height calculated a few kilometres from the coastline (Synolakis 1987), so a minimum value of 1 m should be expected in the most exposed parts of the Moroccan coasts.

Another limit is the lack of record of the precise scenario of the sediment failure. The available record does not help to decipher whether the slide failed as a unique event, or as several, distinct smaller events. The fact that we observe only one large MTD is in agreement with the first hypothesis.
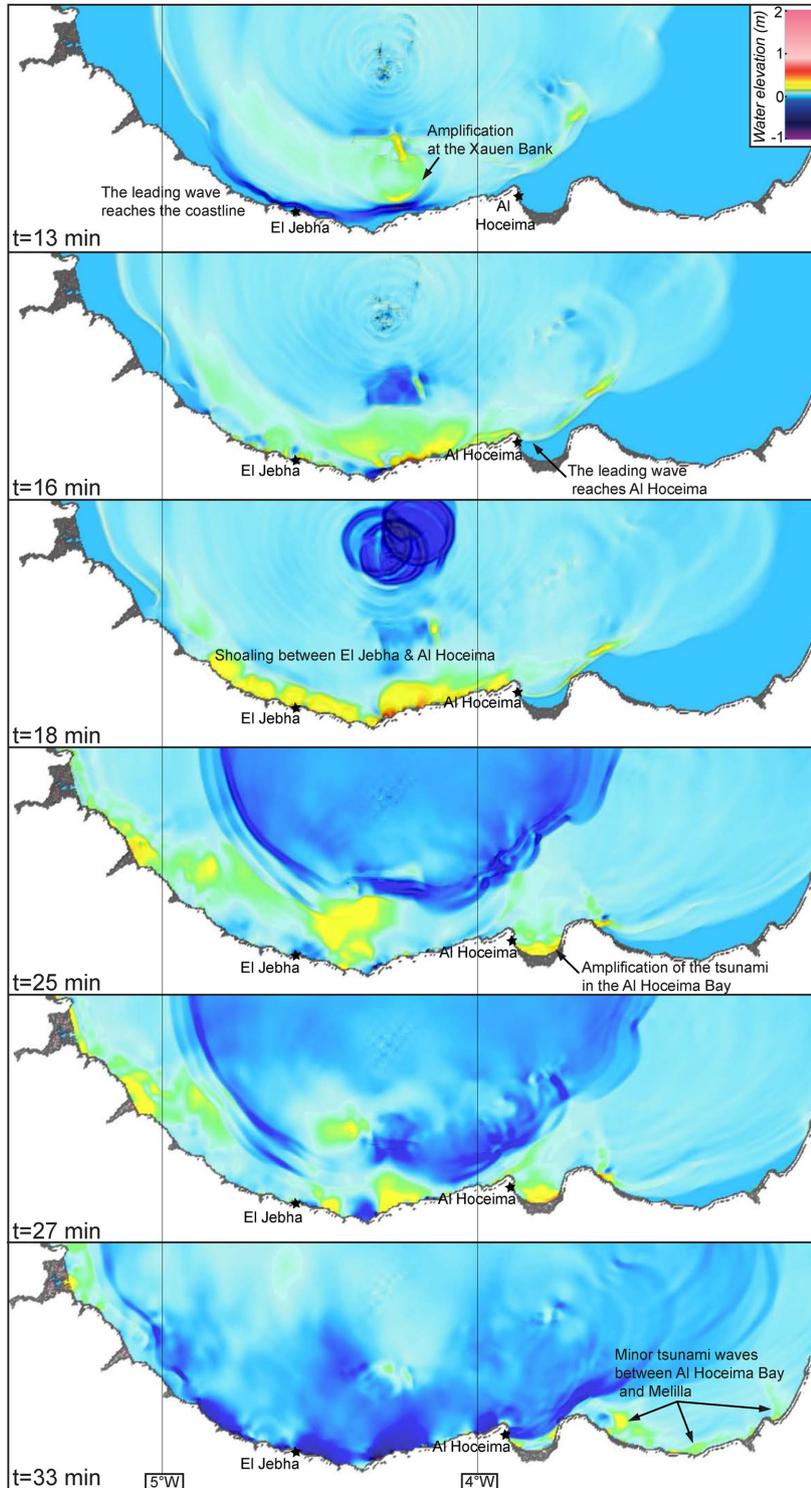
Figure 6. Detailed propagation of the backgoing wave of the tsunami simulated for a landslide with an initial volume of 0.5 km³, a basal friction angle $\varphi = 3.5°$ and a water entrainment coefficient $e_w = 2 \times 10^{-3}$ for the Moroccan coastline, at $t = 13, 16, 18, 25$ and 33 min of propagation.

The lack of geological record of the actual velocity pattern of the slide also leads to strong assumptions on the initial pattern of the tsunami. The initial slide acceleration and its speed strongly impinge on the initial pattern of the tsunami, including the pattern of short wavelengths, and therefore on the subsequent frequency dispersion (Haugen *et al.* 2005). Here, we simply consider an initial acceleration in the first minutes of the slide mo-

tion, reaching values of velocity compatible with the ones estimated for the 1998 Papua-New Guinea landslide. The actual velocity patterns may be more complex, with the peak of acceleration occurring sooner or later, at different water depths. Taking into account a reasonable added mass coefficient would reduce the initial acceleration of the slide by $\sim 10^{-2}$ m s^{-2}, and decrease the elevation of the tsunami at the source (Grilli & Watts 2005).
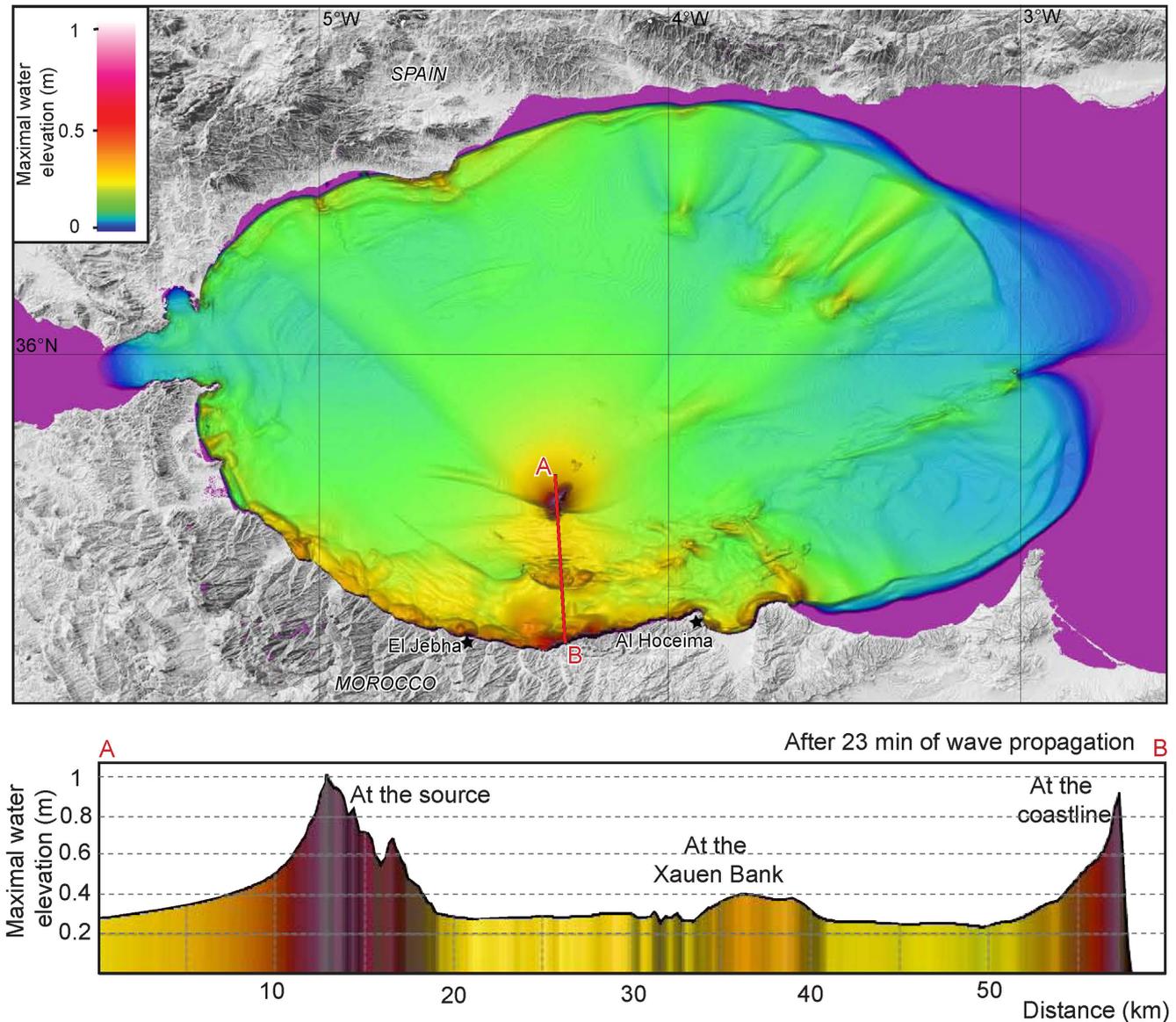
Figure 7. Map of the maximal water heights reached by the tsunami after 23 min of propagation (same parameters as Fig. 6).

The actual velocity of the slide may have been much less than the one considered here. All these effects may result in tsunami with water elevation less important than the ones obtained in our scenarios.

A second-order source of simplification is the non-dispersive numerical model that is not able to account for frequency dispersion inherent in tsunamis with short wavelengths, thus especially for landslide with small volume (on the order of 1 km^3 or less) like the Xauen–Tofiño landslides. It has been shown for the Papua-New Guinea tsunami event of 1998 that dispersion effect becomes significant at ∼50 km from the source, but neglecting dispersion does not lead to major errors in the computation of the tsunami between the source and the coastline (Glimsdal *et al.* 2013), which corresponds to a distance of ∼20 km in that case. As the distance of propagation from the Xauen–Tofiño landslides to the Moroccan coast is short (∼30 km), limited frequency dispersion can be expected, but it depends mainly on the pattern of short wavelengths generated during the slide motion, which cannot be precisely determined due to the lack of information on

the actual slide velocity. Conversely, the tsunami elevations of ∼20 cm calculated at the southern Iberian Peninsula coast are certainly overestimated due to the lack of frequency dispersion in our simulations.

Even if some maximizing (but not excessive) assumptions have been done, the result is that the tsunami threat related to the Xauen–Tofiño landslides is quite moderate. From all the Holocene slide observed, only one is able to produce a tsunami with water elevation reaching 1 m at the Moroccan coast.

Our deterministic approach simply constitutes a first step towards a complete tsunami hazard assessment. The consideration of more complex and more variable slide motion patterns are needed to properly build the probabilistic assessment of the tsunami hazard in this area (Geist & Lynett 2014). Coring of the Holocene MTD is also needed to constrain the frequency of events and support a probabilistic assessment of tsunami hazard in the area (Pope *et al.* 2015). At the timescale of the Pleistocene, a deeper penetrating seismic data set and a better stratigraphic framework of the MTDs will determine where and when larger landslides occurred in the
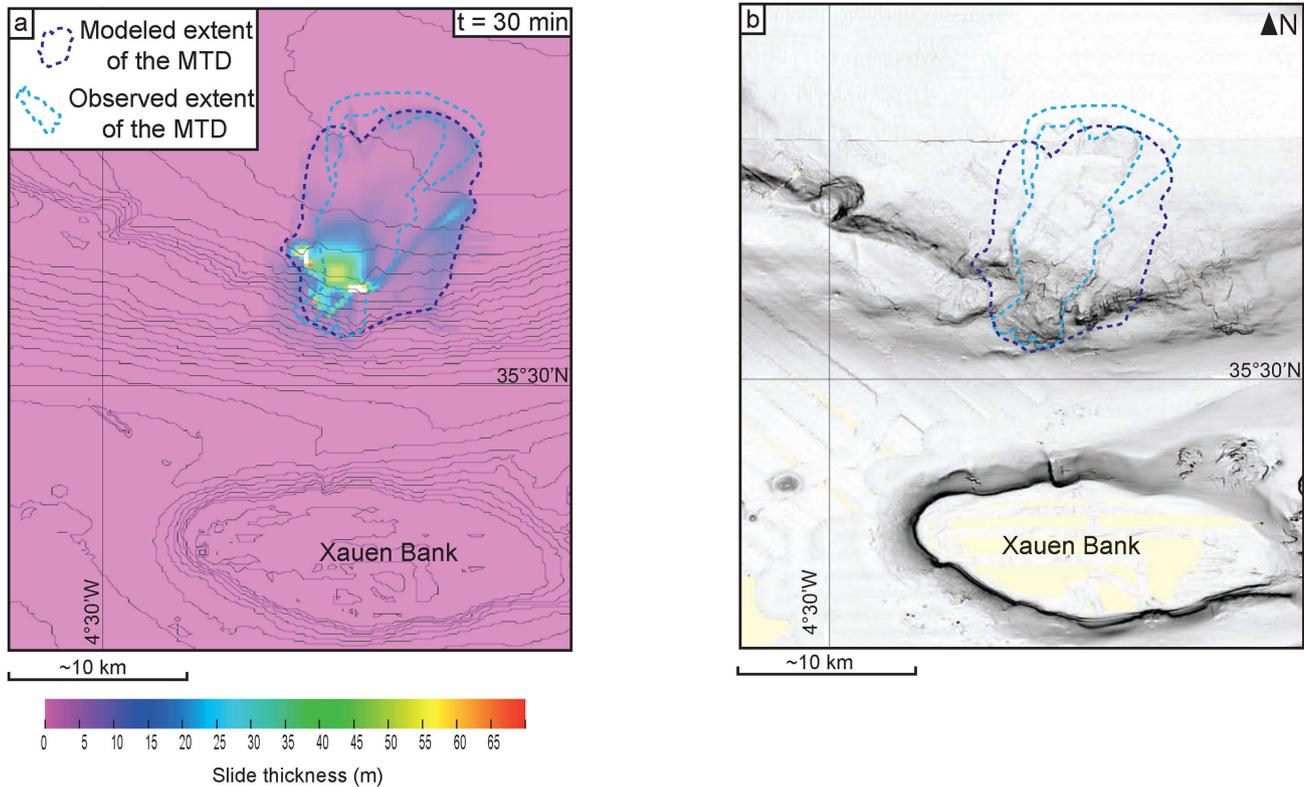
Figure 8. Comparison between (a) the modeled extent and thickness of the slide and (b) the observed extent of the slide on the multibeam shade relief map.

past. This will help to understand if the system is dominated by the variation of one main control factor, or if several control factors interact together making the distribution of MTD random, and the prediction of tsunami hazard complex.

Predicting submarine landslide tsunamis remains difficult because the physical properties of the sediments over the Xauen–Tofiño bank remain unconstrained. For instance, the fact the recent seismic crisis in 2016 January did not trigger a tsunamigenic landslide at the Xauen bank, despite an *a priori* favourable sedimentary context (high sedimentation rates, fluid circulation within the sedimentary pile), highlights the complexity of tectonosedimentary interactions. Precise measurements of the sediment physical properties are therefore needed to determine the slope stability of the Moroccan margin in southern Alboran. Some simple parameters, such as the density of the sediments, need to be carefully addressed as they can play a critical role in the generation of the tsunami (Ma *et al.* 2013).

REFERENCES

Alonso, B., Ercilla, G., Martínez-Ruiz, F., Baraza, J. & Galimont, A., 1999. Plio-Pleistocene sedimentary facies at Site 976, ODP Leg. 161: Depositional history in the Northwestern Alboran Sea, in *Scientific Results Ocean Drilling Program,* Vol. 161, pp. 57–68, eds Zahn, R., Comas, M.C. & Klaus, A.S., Ocean Drilling Program.

Alonso, B. *et al.*, 2012. Caracterización morfo-sísmica de las inestabilidades sedimentarias del sector oriental del mar de Alborán durante le Cuaternario (SO Mediterraneo), *Geo-Temas 13,* pp. 196–199. ISSN: 1576-5172.

Alonso, B. *et al.*, 2014. Quaternary mass-transport deposits on the northeastern Alboran Seamount (SW Mediterranean), in *Submarine Mass Movements and Their Consequences,* Ch. 50, pp. 561–570, ISBN 978-3-319-00971-1, eds Krastel, S. *et al.*, Springer.

Alvarez-Gomez, J.A., Aniel-Quiroga, I., Gonzalez, M. & Otero, L., 2011a. Tsunami hazard at the western Mediterranean Spanish coast form seismic sources, *Nat. Hazards Earth Syst. Sci.,* **11,** 227–240.

Alvarez-Gomez, J.A., Aniel-Quiroga, I., Gonzalez, M., Olabarrieta, M. & Carreño, E., 2011b. Scenarios for earthquake-generated tsunamis on a complex tectonic area of diffuse deformation and low velocity: the Alboran Sea, Western Mediterranean, *Mar. Geol.,* **284,** 55–73.

Alvarez-Marrón, J., 1999. Pliocene to Holocene structure of the eastern Alboran Sea (western Mediterranean), in *Proceedings of the Ocean Drilling Program, Scientific Results,* Vol. 161, pp. 345–355, eds Zahn, R., Comas, M.C. & Klaus, A. Ocean Drilling Program.

Alcrudo, F. & Garcia-Navarro, P., 1993. A high-resolution Godunov-type scheme in finite volumes for the 2D shallow water equations, *Int. J. Numer. Methods Fluids,* **16,** 489–505.

Bache, F., Olivet, J.-L., Gorini, C., Rabineau, M., Baztan, J., Aslanian, D. & Suc, J.-P., 2009. Messinian erosional and salinity crises: view from the Provence Basin (Gulf of Lions, Western Mediterranean), *Earth planet. Sci. Lett.,* **286,** 139–157.

Baraza, J. & Ercilla, G., 1994. Geotechnical properties of near-surface sediments from the northwestern Alboran Sea slope (SW Mediterranean): influence of texture and sedimentary processes, *Mar. Geores. Geotech.,* **12,** 181–200.

Bryn, P., Berg, K., Forsberg, C.F., Solheim, A. & Kvalstad, T.J., 2005. Explaining the Storegga slide, *Mar. Petrol. Geol.,* **22,** 11–19.

Berndt, C., Costa, S., Canals, M., Camerlenghi, A., de Mol, B. & Saunders, M., 2012. Repeated slope failure linked to fluid migration: the Ana submarine landslide complex, Eivissa Channel, Western Mediterranean Sea, *Earth. planet. Sci. Lett.,* **319–320,** 65–74.

Bezzeghoud, M. & Buforn, E., 1999. Source parameters of the 1992 Melila (Spain, $M_w = 4.8$); 1994 Al Hoceima (Marocco, $M_w = 5.8$) and the Mascara (Algeria, $M_w = 5.7$) earthquakes and seismotectonic implications, *Bull. seism. Soc. Am.,* **99,** 359–372.

Blinova, V.N., Comas, M.C., Ivanov, M.K., Pludetkina, E.N. & Matveeva, T.V., 2011. Active mud volcanism in the West Alboran Basin: geochemical evidence of hydrocarbon seepage, *Mar. Petrol. Geol.,* **28,** 1483–1504.

Bourgois, J., Mauffret, A., Ammar, A. & Demnati, A., 1992. Multichannel seismic data imaging of inversion tectonics of the Alboran Ridge (Western Mediterranean Sea), *Geo-Mar. Lett.,* **12,** 117–122.

Bünz, S., Mienert, J., Bryn, P. & Berg, K., 2005. Fluid flow impact on slope failure from 3D seismic data: a case study in the Storegga Slide, *Basin Res.,* **17,** 109–122.

Canals, M. *et al.*, 2004. Slope failure dynamics and impacts from seafloor and shallow sub-seafloor geophysical data: case studies from the COSTA project, *Mar. Geol.,* **213,** 9–72.

Camerlenghi, A., Accettella, D., Costa, S., Lastras, G., Acosta, J., Canals, M. & Wardell, N., 2009. Morphogenesis of the SW Balearic continental slope and adjacent abyssal plain, Western Mediterranean Sea, *Int. J. Earth Sci.,* **98,** 735–750.

Carter, L., Gavey, R., Talling, P.J. & Liu, J.T., 2014. Insights into submarine geohazards from breaks in subsea telecommunication cables, *Oceanography,* **27,** 58–67.

Casas, D., Ercilla, G., Yenes, M., Estrada, F., Alonso, B., García, M. & Somoza, L., 2011. The Baraza slide. Model and dynamics. Special volume "Seafloor mapping for geohazard assessment", *Mar. Geophys. Res.,* **32,** 245–256.

Chalouan, A., Saji, R., Michard, A. & Bally, A.W., 1997. Neogene tectonic evolution of the southwestern Alboran Basin as inferred from seismic data off Morocco, *AAPG Bull.,* **81,** 1161–1184.

Chaytor, J.D., Ten Brink, U.S., Solow, A.R. & Andrews, B.D., 2009. Size distribution of submarine landslides along the U.S. Atlantic margin, *Mar. Geol.,* **264,** 16–27.

Comas, M.C., Platt, J.P., Soto, J.I. & Watts, A.B., 1999. The origin and tectonic history of the Alboran Basin: insights from leg 161 results, in *Proceedings of the Ocean Drilling Program, Scientific Results,* Vol. 161, pp. 555–580, eds Zahn, R., Comas, M.C. & Klaus, A. Ocean Drilling Program.

d'Acremont, E. *et al.*, 2014. High-resolution imagery of active faulting offshore Al Hoceima, Northern Morocco, *Tectonophysics,* **632,** 160–166.

Do Couto, D. *et al.*, 2014. Tectonic inversion of an asymmetric graben: insights from a combined field and gravity survey in the Sorbas Basin, *Tectonics,* **33,** doi:10.1002/2013TC003458.

DoCouto, D. *et al.*, 2016. Tectonic and stratigraphic evolution of the Western Alboran Sea Basin in the last 25 Myrs, *Tectonophysics,* in press, doi:10.1016/j.tecto.2016.03.020.

El Mrabet, T., 2005. The great earthquakes in the Maghreb region and their consequences on man and environment. Edit. CNRST, 2005 (in Arabic with abreged version in English).

Ercilla, G., Baraza, J., Alonso, B., Estrada, F., Casas, D. & Farrán, M., 2002. The Ceuta Drift, Alboran Sea, southwestern Mediterranean, in *Deep-Water Contourite Systems: Modern Drifts and Ancient Series, Seismic and Sedimentary Characteristics,* Geological Society No. 22, pp. 155–170, eds Stow, D.A.V., Pudsey, C.J., Howe, J.A., Faugères, J.-C. & Viana, A.R., Geological Society, London.

Ercilla, G. *et al.*, 2015. Significance of bottom currents in deep-sea morphodynamics: an example from the Alboran Sea, *Mar. Geol.,* in press, doi:10.1016/j.margeo.2015.09.007.

Estrada, F. *et al.*, 2011. Impact of pulsed Atlantic water inflow into the Alboran Basin at the time of the Zanclean flooding, *Geo-Mar. Lett.,* **31,** 361–376.

Estrada, F., Ercilla, G. & Alonso, B., 1997. The tectosedimentary evolution of the Northeastern Alboran Sea during the Plio-Quaternary, *Tectonophysics,* **382,** 423–442.

Fernández-Ibáñez, F., Soto, J.I., Zoback, M.D. & Morales, J., 2007. Present-day stress field in the Gibraltar Arc (Western Mediterranean), *J. geophys. Res.,* **112,** B08404, doi:10.1029/2006JB004683.

Fine, I.V., Rabinovich, A.B., Bornhold, B.D., Thomson, R.E. & Kulikov, E.A., 2005. The Grand Banks landslide-generated tsunami of November 18, 1929: preliminary analysis and numerical modeling, *Mar. Geol.,* **215,** 45–57.

Fukushima, Y., Parker, G. & Pantin, H.M., 1985. Prediction of ignitive turbidity currents in Scripps Submarine Canyon, *Mar. Geol.,* **67,** 55–81.

Galindo-Zaldivar, J. *et al.*, 2016. Active faulting and earthquakes in the central Alboran Sea, in *35th General Assembly of the European Seismological Commission,* ESC2016-614.

Garcia Castellanos, D., Estrada, F., Jiménez-Munt, I., Gorini, C., Fernàndez, M., Vergés, J. & De Vicente, R., 2009. Catastrophic flood of the Mediterranean after the Messinian salinity crisis, *Nature,* **462,** 778–781.

Geist, E.L. & Lynett, P.J., 2014. Source processes for the probabilistic assessment of tsunami hazards, *Oceanography,* **27,** 87–93.

Glimsdal, S., Pedersen, G.K., Harbitz, C.B. & Løvholt, F., 2013. Dispersion of tsunamis: does it really matter? *Nat. Hazards Earth Syst. Sci.,* **13,** 1507–1526.

Gràcia, E. *et al.*, 2012. Acoustic and seismic imaging of the Adra Fault (NE Alboran Sea): in search of the source of the 1910 Adra earthquake, *Nat. Hazards Earth Syst. Sci.,* **12,** 3255–3267.

Grilli, S. & Watts, P., 2005. Tsunami generation by submarine mass failure. I: modeling, experimental validation, and sensitivity analyses, *J. Waterw. Port Coastal Ocean Eng.,* **131,** 283–297.

Hampton, M.A., Lee, H. & Locat, J., 1996. Submarine landslides, *Rev. Geophys.,* **34,** 33–59.

Harbitz, C.B., Løvholt, F., Pedersen, G. & Masson, D.G., 2006. Mechanisms of tsunami generation by submarine landslides: a short review, *Norw. J. Geol.,* **86,** 249–258.

Harbitz, C.B., Løvholt, F. & Bungum, H., 2014. Submarine landslide tsunamis: how extreme and how likely?, *Nat. Hazards,* **72,** 1341–1374.

Haugen, K.B., Løvholt, F. & Harbitz, C.B., 2005. Fundamental mechanisms for tsunami generation by submarine mass flows in idealized geometries, *Mar. Petrol. Geol.,* **22,** 209–217.

Heezen, B.C. & Ewing, M., 1952. Turbidity currents and submarine slumps, and the 1929 Grand Banks Earthquake, *Am. J. Sci.,* **250,** 775–793.

Hernández-Molina, F.J. *et al.*, 2014. Onset of Mediterranean outflow into the North Atlantic, *Science,* **344,** 1244–1250.

Hernández-Molina, F.J., Serra, N., Stow, D.A.V., Llave, E., Ercilla, G. & Van Rooij, D., 2011. Along-slope oceanographic processes and sedimentary products around the Iberian margin, *Geo-Mar. Lett.,* **31,** 315–341.

Heinrich, P., Piatanesi, A. & Hébert, H., 2001. Numerical modelling of tsunami generation and propagation from submarine slumps: the 1998 Papua New Guinea event, *Geophys. J. Int.,* **145,** 97–111.

Iglesias, O. *et al.*, 2012. The BIG'95 submarine landslide-generated tsunami: a numerical simulation, *J. Geol.,* **120**(1), 31–48.

Ioualalen, M., Migeon, S. & Sardoux, O., 2010. Landslide tsunami vulnerability in the Ligurian Sea: case study of the 1979 October 16 Nice international airport submarine landslide and of identified geological mass failures, *Geophys. J. Int.,* **181,** 724–740.

Jiang, L. & Leblond, P.H., 1992. The coupling of a submarine slide and the surface waves which it generated, *J. geophys. Res.,* **97,** 12 731–12 744.

Jolivet, L., Faccenna, C. & Piromallo, C., 2009. From mantle to crust: stretching the Mediterranean, *Earth planet. Sci. Lett.,* **285,** 198–209.

Juan, C. *et al.*, 2016. A new stratigraphy and depositional model for the Pliocene and Quaternary Alboran Basin. Implications for the paleoceanography, *Mar. Geol.,* in press, doi:10.1016/j.margeo.2015.09.007.

Kostic, S. & Parker, G., 2006. The response of turbidity currents to a canyon-fan transition: internal hydraulic jumps and depositional signatures, *J. Hydraul. Res.,* **44,** 631–653.

Koulali, A. *et al.*, 2011. New GPS constraints on active deformation along the Africa-Iberia plate boundary, *Earth planet. Sci. Lett.,* **308,** 211–217.

Kvalstad, T.J., Andresen, L., Forsberg, C.F., Berg, K., Bryn, P. & Wangen, M., 2005. The Storegga Slide: evaluation of triggering sources and slide mechanics, *Mar. Petrol. Geol.,* **22,** 245–256.

Labbé, M., Donnadieu, C., Daubord, C. & Hébert, H., 2012. Refined numerical modeling of the 1979 tsunami in Nice (French Riviera): comparison with coastal data, *J. geophys. Res.,* **117,** F01008, doi:10.1029/2011JF001964.

Lafosse, M., d'Acremont, E., Rabaute, A., Mercier de Lépinay, B., Tahayt, A., Ammar, A. & Gorini, C., 2016. Evidence of Quaternary transtensional tectonics in the Nekor basin (NE Morocco), *Basin Res.,* doi:10.1111/bre.12185.

Lafuerza, S., Sultan, N., Canals, M., Lastras, G., Cattaneo, A., Frigola, J., Costa, S. & Berndt, C., 2012. Failure mechanisms of Ana Slide from geotechnical evidence, Eivissa Channel, western Mediterranean Sea, *Mar. Geol.,* **307–310,** 1–21.

Larouzière, F.D., Bolze, J., Bordet, P., Hernandez, J., Montenat, C. & Ott d'Estevou, P., 1988. The Betic segment of the lithospheric Trans-Alboran shear zone during the Late Miocene, *Tectonophysics,* **152,** 41–52.

Lastras, G., Canals, M., Hughe-Clarke, J.E., Moreno, A., De Batist, M., Masson, D.G. & Cochonat, P., 2002. Seafloor imagery from the BIG'95 debris flow, western Mediterranean, *Geology,* **10,** 871–874.

L'Heureux, J.S. *et al.*, 2013. Stability, mobility and failure mechanism for landslides at the upper continental slope off Vesterålen, Norway, *Mar. Geol.,* **346,** 192–207.

Loget, N. & Van den Driessche, J., 2006. On the origin of the Strait of Gibraltar, *Sed. Geol.,* **188–189,** 341–356.

Løvholt, F. *et al.*, 2014. Modeling potential tsunami generation by the BIG´95 Landslide, in *Submarine Mass Movements and Their Consequences,* pp. 507–515, eds Krastel, S. *et al.*, Springer.

Løvholt, F., Pedersen, G., Harbitz, C.B., Glimsdal, S. & Kim, J., 2015. On the characteristics of landslide tsunamis, *Phil. Trans. R. Soc. A,* **373,** 2053, doi:10.1098/rsta.2014.0376.

Ma, G., Kirby, J.T. & Shi, F., 2013. Numerical simulation of tsunami waves generated by deformable submarine landslides, *Ocean Model.,* **69,** 146–165.

Macías, J., Vázquez, J.T., Fernández-Salas, L.M., González-Vida, J.M., Bárcenas, P., Castro, M.J., Díaz-del-Río, V. & Alonso, B., 2015. The Al-Borani submarine landslide and associated tsunami. A modeling approach, *Mar. Geol.,* **361,** 79–95.

Mangeney, A., Heinrich, P.H., Roche, R., Boudon, G. & Cheminée, J.L., 2000. Modeling of debris avalanche and generated water waves: application to real and potential events in Montserrat, *Phys. Chem. Earth (A),* **25,** 741–745.

Martinez-Garcìa, P., Comas, M., Soto, J.I., Lonergan, L. & Pérez-Hernández, S., 2009. Recent submarine slides in the Alboran Ridge, *Geogaceta,* **47,** 89–92.

Martinez-Garcìa, P., Comas, M., Soto, J.I., Lonergan, L. & Watts, A.B., 2013. Strike-slip tectonics and basin inversion in the Western Mediterranean: the Post-Messinian evolution of the Alboran Sea, *Basin Res.,* **2,** 361–387.

Masson, D.G., Harbitz, C.B., Wynn, R.B., Pedersen, G. & Lovholt, F., 2006. Submarine landslides: processes, triggers and hazard prediction, *Phil. Trans. R. Soc. A,* **364,** 2009–2039.

Mc Adoo, B.G., Pratson, L.F. & Orange, D.L., 2000. Submarine landslide morphology, US continental slope, *Mar. Geol.,* **169,** 103–136.

Micaleff, A., Berndt, C., Masson, D.G. & Stow, D.A.V., 2007. A technique for the morphological characterization of submarine landscapes as ex-emplified by debris flows of the Storegga Slide, *J. geophys. Res.,* **112,** doi:10.1029/2006JF000505.

Mienert, J. & Posewang, J., 1999. Evidence of shallow- and deep-water gas hydrate destabilizations in North Atlantic polar continental margin sediments, *Geo-Mar. Lett.,* **19,** 143–149.

Migeon, S. *et al.*, 2011. Morphology, distribution and origin of recent submarine landslides of the Ligurian Margin (North-western Mediterranean): some insights into geohazard assessment, *Mar. Geophys. Res.,* **32,** 225–243.

Mohammed, F. & Fritz, H.M., 2012. Physical modeling of tsunamis generated by three-dimensional deformable granular landslides, *J. geophys. Res.,* **117,** doi:10.1029/2011JC007850.

Mulder, T. & Cochonat, P., 1996. Classification of offshore mass movements, *J. Sediment. Res.,* **66,** 43–57.

Mulder, T. & Alexander, J., 2002. Abrupt change in slope causes variation in the deposit thickness of concentrated particle-driven density currents, *Mar. Geol.,* **175,** 221–235.

Mulder, T., Savoye, B. & Syvitski, J., 1997. Numerical modelling of a mid-sized gravity flow: the 1979 Nice turbidity current (dynamics, processes, sediment budget and seafloor impact), *Sedimentology,* **44,** 305–326.

Nocquet, J.-M. & Calais, E., 2004. Geodetic measurements of crustal deformation in the Western Mediterranean and Europe, *Pure appl. Geophys.,* **161,** 661–681.

Okal, E.A. & Synolakis, C.E., 2003. A theoretical comparison of tsunamis from dislocations and landslides, *Pure appl. Geophys.,* **160,** 2177–2188.

Omeru, T. & Carthwright, J.A., 2015. Multistage, progressive slope failure in the Pleistocene pro-deltaic slope of the West Nile Delta (Eastern Mediterranean), *Mar. Geol.,* **362,** 76–92.

Papadopoulos, G.A. *et al.*, 2014. Historical and pre-historical tsunamis in the Mediterranean and its connected seas: geological signatures, generation mechanisms and coastal impacts, *Mar. Geol.,* **354,** 81–109.

Pérez-Belzuz, F., Alonso, B. & Ercilla, G., 1997. History of mud diapirism and trigger mechanisms in the Western Alboran Sea, *Tectonophysics,* **282,** 399–422.

Pérouse, E., Vernant, P., Chéry, J., Reilinger, R. & McClusky, S., 2010. Active surface deformation and sub-lithospheric processes in the western Mediterranean constrained by numerical models, *Geology,* **38,** 823–826.

Piper, D.J.W., Cochonat, P. & Morrison, M., 1999. The sequence of events around the epicenter of the 1929 Grand Bank earthquake: initiation of debris flows and turbidity current inferred from sidescan sonar, *Sedimentology,* **46,** 79–97.

Pope, E.L., Talling, P.J., Urlaub, M., Hunt, J.E., Clare, M.A. & Challenor, P., 2015. Are large submarine landslides temporally random or do uncertainties in available age constraints make it impossible to tell?, *Mar. Geol.,* **369,** 19–33.

Rebesco, M., Hernàndez-Molina, F.J., Van Rooij, D. & Wahlin, A., 2014. Contourites and associated sediments controlled by deep-water circulation processes: state of the art and future considerations, *Mar. Geol.,* **352,** 111–154.

Reicherter, K. & Becker-Heidmann, P., 2009. Tsunami deposits in the western Mediterranean: remains of the 1522 Almería earthquake?, *Geol. Soc. Lond., Spec. Publ.,* **316,** 217–235.

Rodriguez, M., Fournier, M., Chamot-Rooke, N., Huchon, P., Zaragosi, S. & Rabaute, A., 2012. Mass wasting processes along the Owen Ridge (NW Indian Ocean), *Mar. Geol.,* **326–328,** 80–100.

Roger, J. & Hébert, H., 2008. The 1856 Djijelli (Algeria) earthquake and tsunami: source parameters and implications for tsunami hazard in the Balearic Islands, *Nat. Hazards Earth Syst. Sci.,* **8,** 721–731.

Roger, J., Hébert, H., Ruegg, J.C. & Briole, P., 2011. The El Asnam 1980 October 10 inland earthquake: a new hypothesis of tsunami generation, *Geophys. J. Int.,* **195,** 1135–1146.

Roveri, M. *et al.*, 2014. The Messinian salinity crisis: past and future of a great challenge for marine sciences, *Mar. Geol.,* **352,** 25–58.

Savage, S. & Hutter, K., 1989. The motion of a finite mass of granular material down a rough incline, *J. Fluid. Mech.,* **199,** 177–215.

Seiqueiros, O.E., Naruse, H., Endo, N., Garcia, M.H. & Parker, G., 2009. Experimental study on self-accelerating turbidity currents, *J. geophys. Res.,* **114,** C05025, doi:10.1029/2008JC005149.

Serpelloni, E., Vannucci, G., Pondrelli, S., Argnani, A., Casula, G., Anzidei, M., Baldi, P. & Gasperini, P., 2007. Kinematics of the western Africa–Eurasia plate boundary from focal mechanisms and GPS data, *Geophys. J. Int.,* **169,** 1180–1200.

Skilbeck, C.G. & Tribble, J.S., 1999. Description, classification, and origin of upper Pliocene-Holocene marine sediments in the Alboran basin, *Proc. Ocean Drill. Program: Sci. Results,* **161,** 83–97.

Somoza, L. *et al.*, 2012. Structure of mud volcano systems and pockmarks in the region of the Ceuta Contourite Depositional System (Western Alboran Sea), *Mar. Geol.,* **332–334,** 4–26.

Stich, D., de Lis Mancilla, F., Baumont, D. & Morales, J., 2005. Source analysis of the M_w 6.3 2004 Al Hoceima earthquake (Morocco) using regional apparent source time functions, *J. geophys. Res.,* **110,** B06306, doi:10.1029/2004JB003366.

Sultan, N., Gaudin, M., Berné, S., Canals, M., Urgeles, R. & Lafuerza, S., 2007. Analysis of slope failures in submarine canyon heads: an example from the Gulf of Lions, *J. geophys. Res.,* **112,** F01009, doi:10.1029/2005JF000408.

Synolakis, C.E., 1987. The run-up of solitary waves, *J. fluid Mech.,* **185,** 523–545.

Tappin, D.R., 2010. Digital elevation models in the marine domain: investigating the offshore tsunami hazard from submarine landslides, *Geol. Soc. Lond., Spec. Publ.,* **345,** 81–101.

Tappin, D.R., Watts, P. & Grilli, S.T., 2008. The Papua New Guinea tsunami of 17 July 1998: anatomy of a catastrophic event, *Nat. Hazards Earth Syst. Sci.,* **8,** 243–266.

Tappin, D.R., Watts, P., McMurtry, G.M., Laffoy, Y. & Matsumoto, T., 2001. The Sissano, Papua New Guinea tsunami of July 1998—offshore evidence on the source, *Mar. Geol.,* **175,** 1–23.

ten Brink, U.S., Chaytor, J.D., Geist, E.L., Brothers, D.S. & Andrews, B.D., 2014. Assessment of tsunami hazard to the U.S. Atlantic margin, *Mar. Geol.,* **353,** 31–54.

ten Brink, U.S., Geist, E.L. & Andrews, B.D., 2006. Size distribution of submarine landslides and its implication to tsunami hazard in Puerto Rico, *Geophys. Res. Lett.,* **33,** L11307, doi:10.1029/2006GL26125.

Torne, M., Fernàndez, M., Comas, M.C. & Soto, J.I., 2000. Lithospheric structure beneath the Alboran Basin: results from 3D Gravity modeling and tectonic relevance, *J. geophys. Res.,* **105,** 3209–3228.

Trifunac, M.D. & Todorovska, M.I., 2002. A note on differences in tsunami source parameters for submarine slides and earthquakes, *Soil Dyn. Earthq. Eng.,* **22,** 143–155.

Twichell, D.C., Chaytor, J.D., ten Brink, U.S. & Buczkowski, B., 2009. Morphology of late Quaternary submarine landslides along the U.S. Atlantic continental margin, *Mar. Geol.,* **264,** 4–15.

Urgeles, R. & Camerlenghi, A., 2013. Submarine landslides of the Mediterranean Sea: trigger mechanisms, dynamics, and frequency-magnitude distribution, *J. geophys. Res.,* **118,** 2600–2618.

Urlaub, M., Talling, P.J., Zervos, A. & Masson, D., 2015. What causes large submarine landslides on low gradient ($<2°$) continental slopes with slow ($\sim$0.15 m/kyr) sediment accumulation?, *J. geophys. Res.,* **120,** doi:10.1002/2015JB012347.

Vanneste, M., Sultan, N., Garziglia, S., Forsberg, C.F. & L'Heureux, J.-S., 2014. Seafloor instabilities and sediment deformation processes: the need for integrated, multi-disciplinary investigations, *Mar. Geol.,* **352,** 183–214.

Van der Woerd, J. *et al.*, 2014. The Al Hoceima M_w 6.4 earthquake of 24 February 2004 and its aftershocks sequence, *J. Geodyn.,* **77,** 89–109.

Vázquez, J.T., Alonso, B., Ercilla, G., Carmen, J., Estrada, F. & Garcia, M., 2013. Mass movement deposits and tectonics relation as a main factor to control the stratigraphical architecture of the South Alboran Basin (Alboran Sea, Western Mediterranean), in *Regional Committee on Atlantic Neogene Stratigraphy (RCANS) Congress: Two decades of Atlantic Neogene study,* Huelva, Abstract Book VRCANS, pp. 46–47, http://hdl.handle.net/10272/7006.

Vázquez, J.T. *et al.*, 2015. Seamounts along the Iberian continental margins, *Bol. Geol. y Minero,* **126,** 483–514.

Viesca, R.C. & Rice, J., 2012. Nucleation of sleep-weakening rupture instability in landslides by localized increase in pore pressure, *J. geophys. Res.,* **117,** B03104, doi:10.1029/2011JB008866.

Ward, S.N., 2001. Landslide tsunami, *J. geophys. Res.,* **106,** 11 201–11 215.

Woodside, J.M. & Maldonado, A., 1992. Styles of compressional neotectonics in the eastern Alboran Sea, *Geo-Mar. Lett.,* **12,** 111–116.